Physics and Chemistry of Minerals (2021) 48:36
https://doi.org/10.1007/s00269-021-01160-8

ORIGINAL PAPER

In situ X-ray diffraction study of chrysotile at high *P–T* conditions: transformation to the 3.65 Å phase

Sergey V. Goryainov[1] · John S. Tse[2] · Serge Desgreniers[3] · Saori I. Kawaguchi[4] · Yuanming Pan[5] · Anna Yu. Likhacheva[1,6] · Maxim S. Molokeev[7,8]

Received: 29 April 2021 / Accepted: 4 September 2021 / Published online: 29 September 2021

Abstract

The behavior of chrysotile $Mg_3(Si_2O_5)(OH)_4$ in water medium at simultaneously high pressure and high temperature was studied by *in situ* synchrotron X-ray diffraction using a diamond anvil cell. In contrast to previous 'dry' experiments, chrysotile in water-saturated conditions undergoes two-phase transitions and exhibits higher thermal stability. At 260 °C / 3.7 GPa the initial chrysotile (phase I) transforms to the 'chrysotile-like' phase II, followed by the appearance of the 'chrysotile-like' phase III at 405 °C / 5.25 GPa. Phase III is characterized by enlarged interlayer distances, presumably resulting from the H_2O intercalation into the interlayer space. During further compression, the 'chrysotile-like' phase III is decomposed to the 10 Å phase $Mg_3(Si_4O_{10})(OH)_2{\cdot}xH_2O$, the 3.65 Å phase $MgSi(OH)_6$, phase D, forsterite, enstatite and coesite or stishovite. The 3.65 Å phase appears at 8.8 GPa / 500 °C. The series of transformations leads to a water deficiency in the system, restricting the complete transformation from the 10 Å phase to the 3.65 Å phase. These data emphasize the crucial role of excess water in the stabilization of the high-pressure hydrous phases. The present study is the first *in situ* observation of sequential transformations of hydrous phases: serpentine → 10 Å phase → 3.65 Å phase, important as a potential water transport mechanism to the deep mantle.

Keywords Chrysotile · Serpentine · High pressure · High temperature · X-ray diffraction · Synchrotron radiation

✉ Sergey V. Goryainov
svg@igm.nsc.ru

John S. Tse
john.tse@usask.ca

Serge Desgreniers
sdesgren@uottawa.ca

Saori I. Kawaguchi
sao.kawaguchi@spring8.or.jp

Yuanming Pan
yuanming.pan@usask.ca

Anna Yu. Likhacheva
alih@igm.nsc.ru

Maxim S. Molokeev
msmolokeev@mail.ru

[1] Sobolev Institute of Geology and Mineralogy, Siberian Branch of the Russian Academy of Sciences, pr. Koptyug 3, Novosibirsk 630090, Russia

[2] Department of Physics, University of Saskatchewan, 116 Science Place, Saskatoon, SK S7N 5B2, Canada

[3] Department of Physics, University of Ottawa, 150 Louis Pasteur, Ottawa, ON K1N 6N5, Canada

[4] Japan Synchrotron Radiation Research Institute, 1-1-1 Kouto, Sayo-cho, Sayo-gun, Hyogo 679-5198, Japan

[5] Department of Geological Sciences, University of Saskatchewan, 114 Science Place, Saskatoon, SK S7N 5E2, Canada

[6] Novosibirsk State University, Pirogov str. 1, 630090 Novosibirsk, Russia

[7] Laboratory of Crystal Physics, Kirensky Institute of Physics, FRC KSC SB RAS, Krasnoyarsk 660036, Russia

[8] Research and Development Department, Kemerovo State University, Kemerovo 650000, Russia

Introduction

Serpentine-group minerals, including antigorite, lizardite, and chrysotile, are the common products of hydrothermal alteration of ultramafic rocks. They are the major hydrous phases in the oceanic lithosphere and contribute to the dehydration processes in subduction zones (Schmidt and Poli 1998; Dobson et al. 2002; Fumagalli and Poli 2005; Ohtani et al. 2018; Gasc et al. 2011, 2017). At serpentine dehydration, the released hydrated fluid triggers partial melting in the volume forming the magma capsules at arc regions that are accompanied by seismic activity (Proctor and Hirth 2016).

Serpentine-group minerals are trioctahedral phyllosilicates that are constructed from 1:1 layers of alternate octahedral and tetrahedral sheets (Wicks and O'Hanley 1988). This stacking varies from the planar structure in lizardite to cylindrically rolled layers in chrysotile and periodic reversals of the polarity of each layer in antigorite. Among the serpentine-group minerals, antigorite is the most stable at high-pressure (H*P*) and high-temperature (H*T*) conditions (Ulmer and Trommsdorff 1995, 1999; Wunder and Schreyer 1997; Bromileyand Pawley 2003; Nestola et al. 2010). Interestingly, kinetics studies of antigorite decomposition revealed an intermediate assemblage of the 'talc-like' phase + forsterite, which appears prior to the formation of the stable anhydrous products, forsterite and enstatite, above 650 °C at 4GPa (Perrillat et al. 2005; Chollet et al. 2011). Note that hydrous phases resulting from serpentine decomposition at high pressure, such as dense hydrous magnesium silicates (DHMS), are of particular interest because they contribute to the H_2O transport into the Earth interiors (Wunder 1998; Ohtani et al. 2004; Ohtani 2015; Komabayashi and Omori 2006; Pamato et al. 2015; Wunder et al. 2011; Welch and Wunder 2012; Mookherjee et al.2015). Among DHMS only the 10 Å phase and the phase A have been detected during antigorite dehydration (Ulmer and Trommsdorff 1995; Inoue et al. 2009).

The upper *P*–*T* stability of chrysotile in the H_2O-saturated system, determined by equilibrium quench experiments, is limited by the decomposition to forsterite + talc /10 Å phase at 500–550 °C (14 GPa) (Ulmer and Trommsdorff 1999). Chrysotile is restricted to lower temperatures of 200–300 °C. Chrysotile is a metastable serpentine variety that can be transformed into antigorite (Evans 2004). The kinetics of this transformation is extremely sluggish. This explains the meta-stability

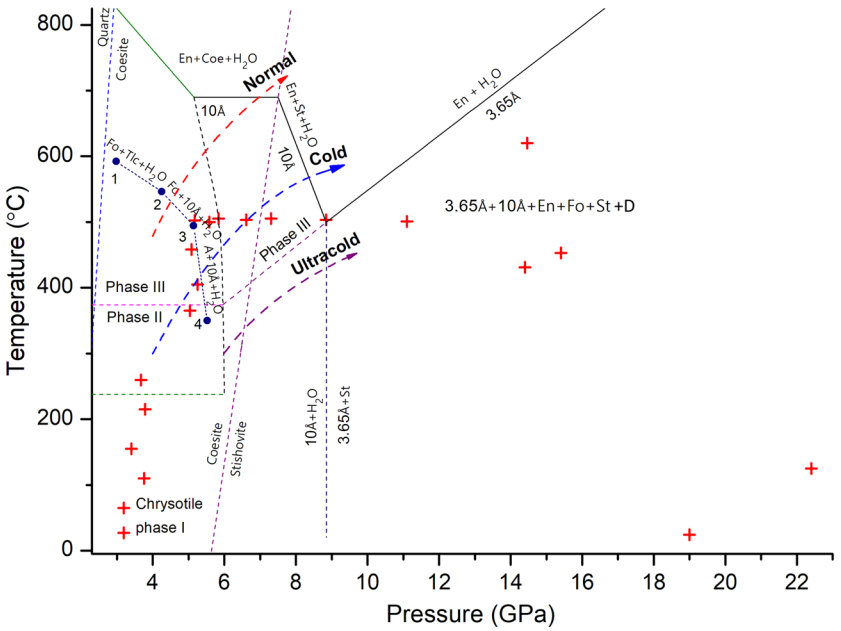

Fig. 1 *In situ* transformations observed in the chrysotile–water system plotted on the *P*–*T* plane. Initial chrysotile (phase I) is transformed to the 'chrysotile-like' phases II and III. The 10 Å phase, the 3.65 Å phase, enstatite (En), forsterite (Fo), stishovite (St), and coesite (coe) are products of chrysotile decomposition. Geotherms are shown be dashed lines with arrows: Normal (red), Cold (blue), and Ultracold (violet), example of Tonga locality (Syracuse et al. 2010). Curves corresponding to the stability fields of the 10 Å and 3.65 Å phases are plotted (Pawley and Wood 1995; Chinnery et al. 1999; Pawley et al. 2011; Peacock and Wang 1999) and corrected in accordance to transformations observed in the present chrysotile–water system at quasi-equilibrated conditions. The dashed broken line (navy color) with point numbers 1–4 exhibits the stability boundary of chrysolite determined by equilibrium quench experiments (Ulmer and Trommsdorff, 1999): at/above broken line (higher ~ 4 GPa / 500 °C) serpentine is decomposed by means: Chrysolite → forsterite + 10 Å phase + H2O. The set of phases (3.65 Å + 10 Å + En + Fo + St + D) is observed above ~ 9 GPa

of chrysotile up to about 400 °C as reported from both field observations and experimental data (e.g.,Mellini et al. 1987; Chernosky et al. 1988). Therefore, chrysotile, a widespread alteration mineral of ultramafic rocks, deserves attention as a possible participant of metamorphic processes during the subduction of hydrated peridotites. In this connection, we investigate the H*P*–H*T* behavior of chrysotile in the presence of water by *in situ* methods, which have not been studied so far. Here, we present the first *in situ* H*P*–H*T* synchrotron X-ray diffraction investigation of chrysotile and its decomposition products under H_2O-saturated conditions up to 22 GPa and 620 °C (Fig. 1).

Experimental details

Sample investigated

A sample of chrysotile from Thetford Mines (Quebec, Canada) was used as the starting material in this study. X-ray fluorescence analysis of this sample yielded a formula $Mg_{2.93}Fe_{0.05}Al_{0.06}Si_{1.96}O_5(OH)_4$, which deviates from the ideal formula $Mg_3(Si_2O_5)(OH)_4$ with minor amounts of Al_2O_3 and FeO but is consistent with the average electron-microprobe data of Thetford chrysotile in veins (Cogulu and Laurent 1984). The sample was ground to a powder with a particle size < 2 μm. X-ray diffraction (XRD) patterns of the Thetford sample in the DAC show that, apart from chrysotile, there is a small amount of quartz (Table 1), which is typical for chrysotile samples from Thetford. In addition, a small sphere (~ 2 μm in diameter) of corundum (ruby) was inserted in the DAC as an auxiliary pressure indicator.

In situ X-ray diffraction

X-ray diffraction measurements were performed at the BL10XU beamline of the SPring-8 synchrotron radiation facility (Hyogo, Japan). The BL10XU beamline has an optical hutch and two experimental hutches. One experimental

Table 1 *P–T–t* scheme of the experiments in the chrysotile–water system

Observation No	Time (min)	*P* (GPa)	*T* (°C)	Phase I = Ctl	Phase II	Phase III	10 Å phase	3.65 Å phase	Ice	Enstatite	Forsterite	Coe/st
1	0	3.19	27	+	–	–	–	–	+	–	–	–
2	62	3.19	65	+	–	–	–	–	+	–	–	–
3	234	3.76	110	+	–	–	–	–	+	–	–	–
4	317	3.4	155	+	–	–	–	–	+	–	–	–
5	355	3.78	215	+	–	–	–	–	–	–	–	–
6	418	3.67	260	–	+	–	–	–	+	–	–	–
7	470	5.04	365	–	+	–	–	–	+	–	–	–
8	505	5.25	405	–	(+)	+	–	–	–	–	–	–
9	542	5.08	458	–	–	+	–	–	–	–	–	–
10	569	5.17	502	–	–	+	–	–	–	–	–	–
11	617	5.84	505	–	–	+	+	–	–	+	+	+
12	645	6.61	503	–	–	+	+	–	–	+	+	+
13	672	5.58	500	–	–	+	+	–	–	+	+	+
14	703	7.3	505	–	–	+	+	–	–	+	+	+
15	731	8.84	503	–	–	(+)	+	+	–	+	+	+
16	755	11.1	501	–	–	–	+	+	–	+	+	+
17	768	14.4	431	–	–	–	+	+	–	+	+	+
18	794	15.4	453	–	–	–	+	+	–	+	+	+
19	834	14.46	620	–	–	–	+	+	–	+	+	+
20	870	22.4	125	–	–	–	+	+	–	+	+	+
21	910	19	24	–	–	–	+	+	–	+	+	+

Abbreviations and signs are: chrysotile (Ctl); plus, + phase is available; minus, – phase is absent; plus is given in parentheses, (+) that phases are in minor or remnant amounts; ice VII (ice); coesite (coe) or stishovite (st) above 7 GPa. Note that minus sign marks the absence of the phase only in small volume, where X-ray diffraction signal was collected, whereas the DAC working volume is larger and, hence, may include this phase. Detected impurity phases (corundum, quartz, Re, and Au metals) are described in the text and shown in XRD pattern figures. Pressure was measured using the gold state equation (Sokolova et al. 2013). Accuracy of measurements is following: pressure ± 0.1 GPa and temperature ± 1.5 °C. Superheated ice VII is observed at points 6 and 7

hutch used is optimized for high-pressure and high-temperature experiments using a laser or resistively heated membrane DAC (Hirao et al. 2020). An X-ray beam of wavelength $\lambda = 0.41427$ Å (energy 29.9 keV) was monochromatized with a Si(111) double crystal and focused to the spot of about 20-µm in diameter using X-ray refractive lenses. The X-ray beam was focused to the center of the sample and the patterns (Bragg's circles) were recorded with an image plate (IP) detector (Rigaku RAXIS-IV). The recorded diffraction patterns were integrated with the Fit2D software (Hammersley et al. 1996).

Analysis of XRD patterns was performed with the Rietveld method, using the Topas 4.2 software (Bruker AXS TOPAS V4 2008). Rietveld refinements of the initial phases were carried out, using an anisotropic preferred orientation model because some peaks were unusually strong. These peaks were probably due to the presence of microcrystals in the powder. The final refinement was stable and led to relatively low R-factors. The refined cell parameters and cell volume of the main phase (chrysotile) were found. Almost all peaks on the patterns were indexed by several phases, for instance, point 1 in Table 1: chrysotile (wt. ~ 60%), corundum (wt. ~ 15%), and quartz (wt. ~ 10%) and ice VII (wt.15%). Based on these XRD data and Rietveld refinements and taking into account the ratio between the XRD measured volume and the working volume of the DAC, we estimated the total contents of corundum and quartz to be < 2 wt% and < 1 wt%, respectively.

High-pressure–high-temperature devices, P-calibrant and chronology of the experiments

H*P*–H*T* were generated by a resistively heated membrane (Bassett type) DAC (JASRI production, Hyogo, Japan) with a pair of 500 µm culet diamonds and a molybdenum resistive heater (Bassett et al. 1993). The chrysotile sample was mixed with a small amount of distilled water. Small spheres of gold (diameter of ~ 5 µm) were used as the pressure calibrant at temperatures above 50 °C.

The sample temperature was controlled by a Pt/Rh 90%/10%-Pt thermocouple mounted at each anvil nearby the gasket. The difference between the two thermocouples did not exceed ± 1 °C. The temperature deviation measured by the thermocouples in the resistively heated DAC was estimated to be ± 1.5 °C (Bassett et al. 1993). Pressure was measured using the equation of state of gold (Sokolova et al. 2013) with an accuracy of ± 0.1 GPa (these data are given in Table 1 and Figures). Before XRD measurements at low temperature (20–50 °C), the pressure was estimated using the ruby luminescence method (Mao et al. 1986). The *P*–*T* parameters of the *in situ* experiment are given in Table 1 and Figs. 1, 2, 3. The XRD pattern at each experimental point was recorded for about 20 min. The chronology of the experiments is presented in Table 1 and Fig. 2.

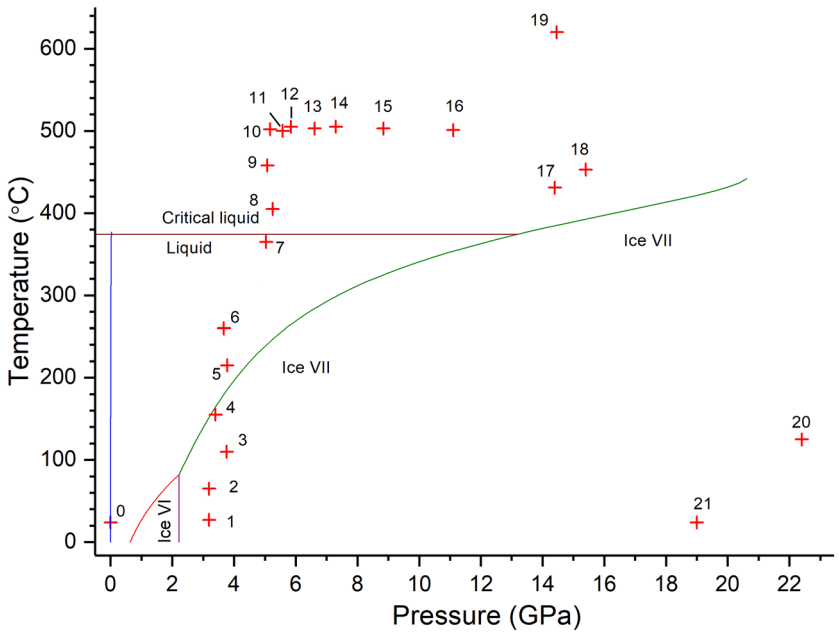

Fig. 2 *P*–*T* diagram of water and the *P*–*T* path of our experiments in the chrysotile–water system (numbered crosses). Solid boundary lines are plotted according to the data (Fletcher, 1970; Hernandez and Caracas, 2018)

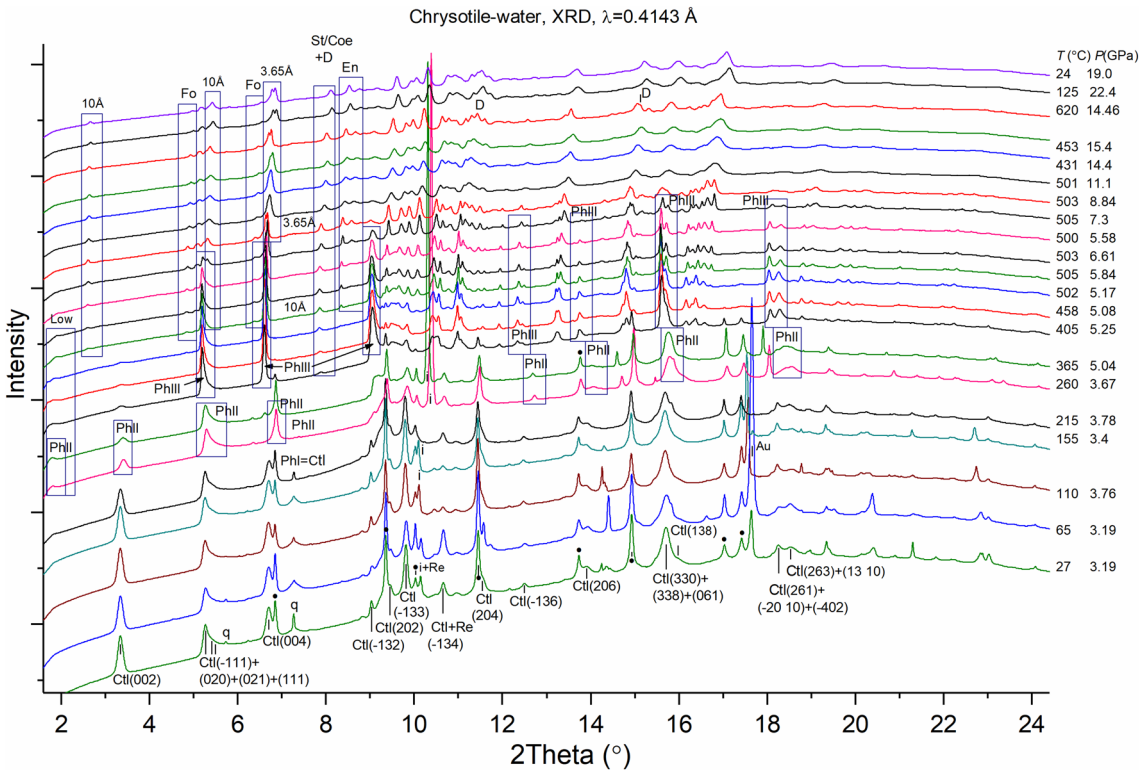

Fig. 3 *In situ* synchrotron X-ray diffraction patterns of the chrysotile–water system recorded at pressure up to 22.4 GPa and temperature up to 620 °C. Wavelength of synchrotron X-ray beam is equal to 0.4143 Å. Peaks of chrysotile (Ctl), phases I–III (PhI–PhIII), forsterite (Fo), enstatite (En), 10 Å phase (10 Å), 3.65 Å phase (3.65 Å), phase D (D) corundum (•), ice VII (i), quartz (q), Re and Au metals are marked correspondently. Characteristic peaks of selected phases are framed. 'Low' frame highlights the XRD anomalies in the low-angle range (see details in Fig. 4). Chrysotile (*hkl*)-peaks and corundum peaks are marked on the first XRD pattern. The *P–T* points of subsequent phase formations are marked in the central part (at ~ 7°): phase II at 3.67 GPa / 260 °C; phase III at 5.25 GPa / 405 °C; 10 Å phase at 5.84 GPa / 505 °C and 3.65 Å phase at 8.84 GPa / 503 °C

Results

An overview of the XRD patterns collected from the chrysotile + water system at $P = 0$–22.4 GPa and $T = 20$–620 °C is given in Fig. 3. The XRD data reveal several transformations of chrysotile and the decomposition reactions plotted in a *P–T* diagram (Fig. 1). The characteristic peaks of chrysotile and its decomposed phases are identified to follow changes in the diffraction patterns (Figs. 3, 4, 5, 6, 7). Before describing the changes observed in chrysotile in detail, it is worthy to characterize the state of the H_2O medium throughout the *P–T* path of the experiments. For this purpose, we plotted the experimental *P–T* points on the H_2O phase diagram (Fletcher 1970; Hernandez and Caracas 2018; Fig. 2) and compared it with the diffraction data in Fig. 3. At low temperatures below 215 °C (3.8 GPa) the XRD patterns contain weak peaks of ice VII, for instance, at $2\theta = 10.13°$, 14.93°, and 17.63° at 3.19 GPa / 27 °C, indicating the presence of excess water in the load. Additional three peaks at 10.38°, 14.98° and 18.05° arise at 3.7 GPa / 260 °C and remain up to 5 GPa / 365 °C; these Bragg reflections belong to the high-pressure ice VII (Fig. 3). This superheated ice VII exhibits a similar shift in the X-ray reflections and appears within the stability field of liquid water near the ice VII—liquid boundary (Fig. 2, points 6 and 7). The sudden appearance of the ice VII at 3.7 GPa / 260 °C could be explained as the result of partial melting of the ice and water transport from the outer zones to the central zone of the DAC. We assume that the superheated ice VII is the result of solidification of the H_2O–SiO_2–MgO solution arising from the partial dissolution of chrysotile and the presence of a small amount of quartz impurity (Table 1). Within the *P*–T range of 3.6–5 GPa / 260–360 °C, the water medium probably consists of a mixture of ice and liquid. Upon the further temperature rise to 400 °C, the system enters the stability field of the supercritical fluid, which is manifested by the disappearance of the ice VII peaks (Fig. 3). Note that, on temperature release down to 125 °C at 22 GPa, the ice peaks did not reappear, which indicates the absence of excess water in the sample.

The XRD patterns (Fig. 3) show that the initial chrysotile (phase I, PhI) transforms to the first intermediate phase II (PhII) at $T = 260$ °C and $P = 3.7$ GPa. A new low-angle

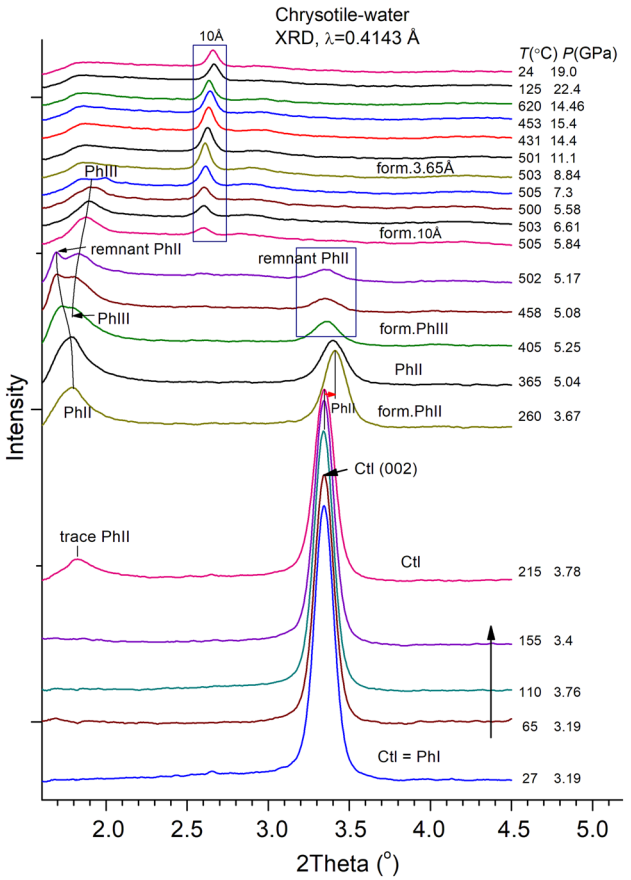

Fig. 4 *In situ* synchrotron X-ray diffraction patterns in the low-angle range of the chrysotile–water system recorded at pressure and temperature up to 22.4 GPa / 620 °C. These patterns are corrected by subtraction of the background taken in the form of smoothed first patterns in the range of 1.6–2.5°. Peaks of (002) chrysotile (Ctl), designated as phase I (PhI), and 'chrysotile-like' phases II and III (PhII and PhIII) are marked with label, black small arrow, and vertical straight line or the curves connecting the peak maximums. These two nearly vertical curves exhibit the shift of two low-angle peaks (one of the phase II and other of the phase III) at increasing *P–T* parameters. Formation of the H*P* phases PhII and PhIII, as well as the 10 Å and 3.65 Å phases are labeled by the word 'form.' Large vertical arrow shows the chronological direction of the experimental *P–T* path

reflection characterizes this phase at 2θ = 1.793° (embedded in the 'low' frame in Figs. 3 and 4), as well as by some changes in the positions and intensities of other reflection peaks (Table 1). The next 'chrysotile-like' phase III (PhIII) appears at 5.25 GPa / 405 °C and is stable up to 7.3 GPa / 500 °C. Phase III is characterized by the appearance of the intense peak at 9.06° (Fig. 3) and appreciable shifts of the main peaks of phase II at 5.30° and 6.864° to lower angles at 5.20° and 6.607°, respectively (Fig. 5).

Figure 4 shows changes in the low-angle range of the XRD patterns. A major difference is the appearance of the low-angle peaks at 2θ = 1.7–2°, nearly coinciding in phases II and III. This low-angle peak of phase III decreases along with the appearance of the10 Å phase as a decomposition product, and it completely disappears before the onset of the 3.65 Å phase formation. Secondly, the intensity of the phase I peak (002) at ~ 3.35° abruptly decreases upon the phase transition I → II and continuously attenuates at higher *P–T* conditions. It completely disappears when the 10 Å phase is formed. The corresponding frame labeled as 'remnant PhII' in Fig. 4 marks the *P–T* range, where phases II and III coexist.

Figure 5 shows the changes in the XRD patterns in selected middle-angle ranges during the two transitions between the 'chrysotile-like' phases I–II and II–III. Blue arrows indicate the shift to higher diffraction angles at the phase I → II transition. The diffraction pattern in the range of 6.5–7° is deconvoluted to show the relationship between the diffraction peaks in phases I (reflection (004)) and II. In the pattern recorded at 3.67 GPa / 260 °C, the Bragg diffraction at ~ 6.8° is interpreted as the imposition of a narrow corundum peak and a broad peak of phase II. At 3.4–3.78 GPa and 155–215 °C the reflection (004) of chrysotile phase I is 2.5 times wider compared to the neighbouring peak of corundum. Assuming this ratio is the same in phase II and using deconvolution, we can distinguish phase II and corundum peaks.

Figure 8 summarizes the results of Rietveld refinements of the XRD patterns: the dependence of the chrysotile unit-cell volume on temperature at *P–T* parameters shown in Table 1. Points –-4 measured at increasing temperature and relatively small deviations of pressure and represent the thermal expansion of the chrysotile sample. At point 5 (Fig. 8), the volume decreases sharply despite increasing temperature up to 60 °C. The volume reduction could be associated with the beginning of the transition from phase I to II. These data further support the presence of the transition I–II with decreasing unit-cell volume.

The diffraction peaks shift noticeably to lower angles upon the II–III phase transition, marked by red arrows in Fig. 5. The number of strong and moderate Bragg reflections in phase III is more than in phase II. Frames in Fig. 3 show only selected reflections of phase III, which are related to phases I and II and but do not overlap with the other phases (Figs. 3, 4, 5). Besides these correlated reflections, many unidentified reflections appeared at the phase transition II → III (Fig. 3, Table 1). The appearance of additional peaks in the diffraction pattern may indicate a reduced symmetry accompanying by the II → III phase transition. All characteristic and additional peaks of phase III are detected in a wide *P–T* range and disappear at 8.84 GPa / 503 °C, when the 3.65 Å phase is formed.

Another notable feature is the appearance of the silica phase, coesite, simultaneously with the phase III at 5.25 GPa / 400 °C (Fig. 3; Table 1). As mentioned before, free silica was initially present in the sample as quartz impurity. At

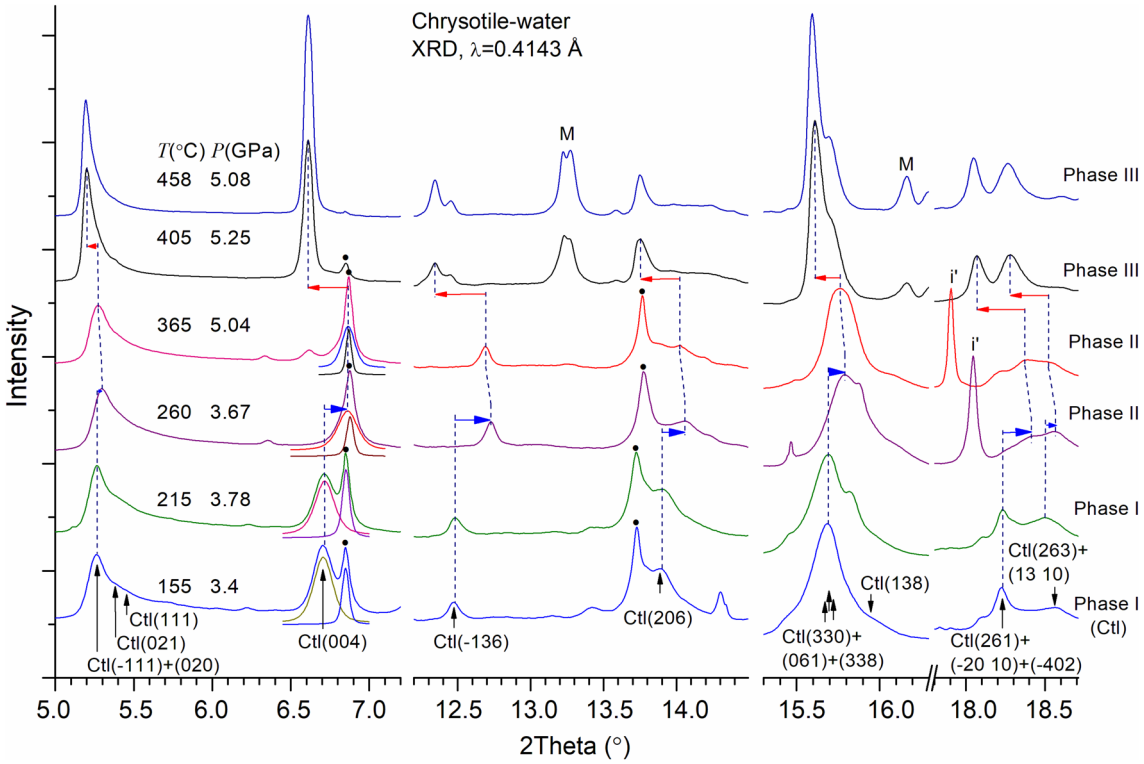

Fig. 5 *In situ* synchrotron X-ray diffraction patterns in selected middle-angle ranges of the chrysotile–water system presented at the pressure range of 3.4–5.25 GPa and the temperature range of 155–458 °C. Chrysotile (Ctl), corundum (•), and ice VII (i) and the phase mixture (M) are marked. These M peaks include the overlapped reflections of enstatite, forsterite, phase III, and unidentified phases. Blue arrows show step-wise changes of the peaks at transition from phase I to II. Red arrows exhibit step-wise changes of the peaks at transition from phase II to III. The peak deconvolution is used to distinguish wide chrysotile (004) peak in the phase II that is overlapped with a narrow corundum peak

3.6–5 GPa and 260–400 °C, it completely dissolves, apparently due to the ice melting and the formation of a supercritical aqueous fluid (Fig. 2). Since the temperature of this fluid becomes even higher in the subsequent experiments, the appearance of coesite cannot be explained by a sudden change of SiO_2 solubility in the fluid. Coesite remains up to about 7GPa, when it is replaced by stishovite; both of these silica phases have a dominant reflection at $2\theta \sim 8°$ (Fig. 3).

Upon compression to 5.8 GPa at ~ 500 °C, the 'chrysotile-like' phase III begins to decompose, which is evident from the appearance of the characteristic peaks of three new phases: the 10 Å phase, enstatite and forsterite (Fig. 3, Table 1). Forsterite is a common decomposition product of serpentine (Ulmer and Trommsdorff 1995, 1999). The dashed broken line in Fig. 1 with breakpoints 1–4 shows the stability boundary of chrysotile determined with equilibrium experiments using *ex situ* products (Ulmer and Trommsdorff 1999). This broken boundary (Fig. 1) corresponds to the serpentine decomposition by following reactions: 1–2 line, Chrysotile → Forsterite + talc + H_2O; 2–3 line, Chrysotile → Forsterite + 10 Å phase + H_2O; 3–4 line, Chrysotile → Phase A + 10 Å phase + H_2O. Forsterite was detected at *P–T* conditions corresponding to the data from a previous work (Ulmer and Trommsdorff 1999), while phase A was not observed in the present chrysotile–water experiments (Figs. 1 and 3). Analysis of experimental XRD patterns (Figs. 3, 5 and 7) shows an apparent distinction between phases III and A, compared with an earlier report (Holl et al. 2006). The stability field of the 'chrysotile-like' phase III partially overlaps with that of phase A (see Fig. 1), different from Fig. 4 of Ulmer and Trommsdorff (Ulmer and Trommsdorff1999). The discrepancy in the products of serpentine decomposition may be explained by the different amounts of excess water in the chrysotile–water system, the different experimental conditions (*in situ* in the present experiments), and the possible meta-stability of the new phase III.

Comparison of XRD patterns demonstrates that the phase III is clearly different from known hydrous phases A, E, D, and wadsleyite (Kudoh and Inoue 1999) (Fig. 7). The phase III XRD pattern also differs from other known hydrous phases in the SiO_2–MgO–H_2O and SiO_2–Al_2O_3–MgO–H_2O systems: humite, chondrodite, superhydrous phase B, and δ-phase (Sclar et al. 1965; Liu et al. 2019). Thus, one can consider the phase III as a new hydrous phase. Probably, the

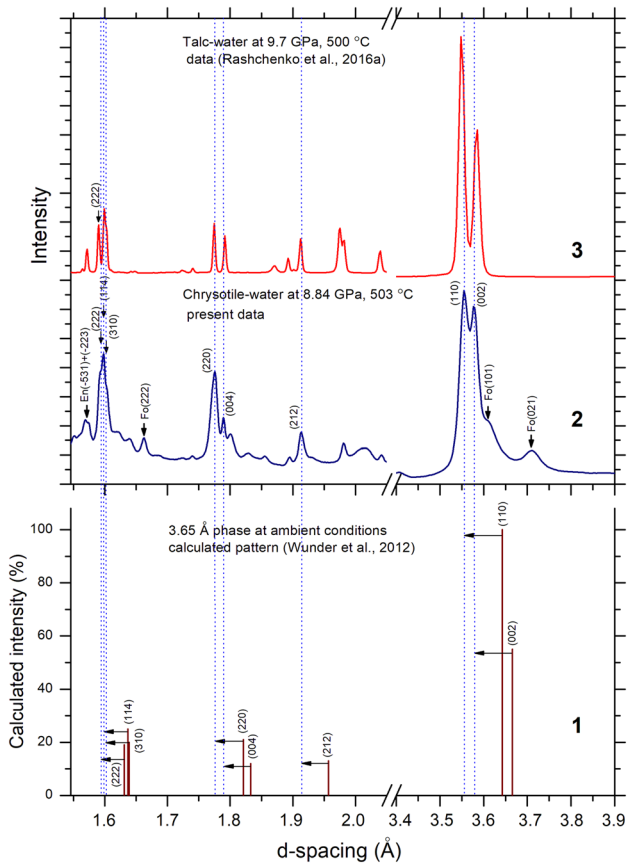

Fig. 6 Identification of the 3.65 Å phase in the X-ray diffraction patterns plotted as intensity versus *d*-spacing: comparison of the calculated pattern at 1 bar (Wunder et al. 2012) (1) with experimental patterns recorded in the present chrysotile–water system at 8.84 GPa / 503 °C (2) and in the talc-water system at 9.7 GPa / 500 °C (Rashchenko et al. 2016a) (3). All representative diffraction (*hkl*)-peaks of the 3.65 Å phase labeled in (1) are identified in the present experimental pattern (2). Peaks of the 3.65 Å phase in the pattern (3), including the resolved (222)-peak, are close to those of the pattern (2) marked by vertical dashed lines. Horizontal arrows indicate the shifts of the reflections at compression and heating. The peaks of enstatite (En) and forsterite (Fo) are also labeled in the pattern (2)

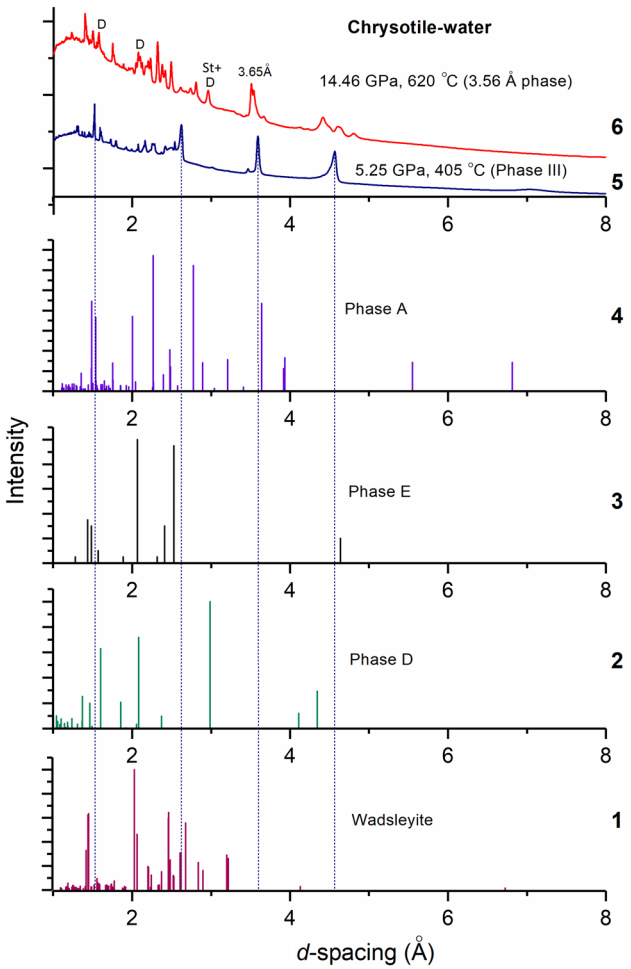

Fig. 7 Comparison of the present X-ray diffraction patterns plotted as intensity versus *d*-spacing of the phase III (5) and the 3.65 Å phase (6), where each phase is dominant in the chrysotile–water system (Figs. 1 and 2, Table 1), with the patterns of hydrous phases: wadsleyite (1), phases D (2), E (3) and A (4). X-ray diffraction patterns (1–4) are plotted, using the data for wadsleyite (Kudoh and Inoue 1999), phase A (Holl et al. 2006), phase D (Yang et al. 1997) and phase E (Kanzaki 1991). Vertical dashed lines show main peaks of phase III in pattern (5). Strong doublet peak of dominant 3.65 Å phase and peaks of impurity phase D are labeled in pattern (6)

reason that this phase was absent was that DHMS (besides phase A) and other hydrous phases were grown at higher *P*–*T* conditions compared with phase III. For instance, phase E (Crichton and Ross 2000; Kanzaki 1991) and phase D (Yang et al. 1997; Frost and Fei 1998; Ghosh and Schmidt 2014; Liu et al. 2019), hydrous δ-phase AlOOH–$MgSiO_2(OH)_2$ (Ohira et al. 2014) appeared at significantly higher *P*–*T* conditions.

Upon further pressure increase to ~ 8.8 GPa at 500 °C, phase III has completely decomposed, with the appearance of the diffraction peaks of the 3.65 Å phase (Figs. 3 and 6) and the phase D (Fig. 7). Note that phase D is a typical product in mixture with the 3.65 Å phase from synthesis experiments proved by XRD data (Borodina et al. 2020). Note that content of D phase remains controversial because of overlapping main reflections with peaks of other phases: the most intensive peak at $2\theta \sim 8°$ is covered by stishovite peak (Fig. 3).

The Bragg reflections of the 3.65 Å phase, highlighted in the frame in Fig. 3, are followed to the highest *P*–*T* conditions. In addition, the characteristic reflections of the 3.65 Å phase from the chrysotile–water system (Fig. 6) are compatible with the calculated pattern (Wunder et al. 2012) and the experimental pattern of this phase from the talc–water system (Rashchenko et al. 2016a). In the range of $P = 7$–15 GPa and $T = 500$–620 °C, the relative quantities of the 3.65 Å and 10 Å phases remain nearly constant, whereas forsterite

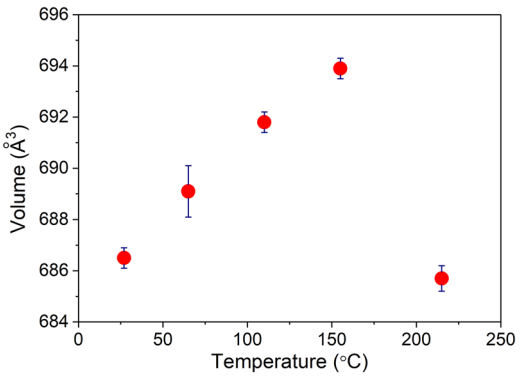

Fig. 8 The chrysotile unit-cell volume (Å^3) versus temperature. Points (Table 1) are measured at P(GPa) – T (°C) conditions: 3.19 27; 3.19 65; 3.76 110; 3.4 155; 3.78 215, that is, pressure is slightly variable. Volume depends nearly linearly on temperature at points 1–4, then at point 5 it sharply drops that is related to the onset of the transition of chrysotile phase I to II. Bars show the uncertainty of volume determination

gradually disappears. The enstatite content has increased notably due to the consumption of forsterite by the reaction with excess SiO_2. However, the coesite/stishovite peak intensity remains constant or even slightly increased, which indicates an appreciable amount of excess SiO_2.

The set of phases (3.65 Å + 10 Å + En + Fo + St + D) is observed in wide *P–T* range, above ~ 9 GPa (Fig. 1). The presence of the 3.65 Å phase is evident by comparable analysis of XRD patterns in Figs. 3 and 6, its *P–T* range observed here is in accordance to the available data (Sclar and Morzenti 1971; Wunder et al. 2011; Welch and Wunder 2012; Mookherjee et al. 2015). Interestingly, this assemblage of six minerals obviously violates the phase rule for the three-component SiO_2–MgO–H_2O system. This apparent violation may be explained by either kinetic processes (i.e., metastable crystallization) or the investigated system containing additional components such as Al_2O_3 and FeO. Aluminum in our experiments comes from not only as a minor constituent in initial chrysotile but also the addition of ruby as a pressure calibrant at low temperatures, which was dissolved at ~ 400 °C / 5GPa (Fig. 3).

The water medium in different *P–T* ranges is revealed as liquid, critical (supercritical) fluid and ice VII (see Fig. 2). Based on the Rietveld analysis of XRD data, we estimated the ice VII content of ~ 15 wt.% in the mixture of chrysotile–corundum–quartz–ice at the first *P–T* point (Table 1). Ice was detected by XRD at low *P–T* (Table 1), but not found at high *T–P* (at $P > 9$ GPa). This result proves the absence of excess water in the system at the last conditions. Moreover, the 3.65 Å phase exhibits broadened reflections in many XRD patterns (Fig. 3), which can be explained from the non-hydrostatic conditions caused by the absence of a water medium.

In summary, *in situ* experiment reveals the H*P*–H*T* induced the transformation of chrysotile to two intermediate 'chrysotile-like' phases II and III and subsequent decomposition to the 10 Å and 3.65 Å DHMS phases. The observed transformations are plotted on the *P–T* graph (Fig. 1), along with equilibrium curves for the reactions involving chrysotile, 10 Å and 3.65 Å phases (Pawley and Wood.

1995; Pawley et al. 2011; Rashchenko et al. 2016a). Dashed curves mark the corresponding *P–T* regions of chrysotile phases II and III in Fig. 1. The upper *P–T* stability limit of chrysotile (phase III) is determined by the reaction 'chrysotile → 10 Å phase + forsterite + H_2O', which is detected to start from 500 °C / 5.8 GPa (Fig. 3). The 3.65 Å phase forms at 8.8 GPa / 500 °C, which also agrees with the available *P–T* data on the reaction '10 Å phase + H_2O → 3.65 Å phase + stishovite' (Pawley et al. 2011; Rashchenko et al. 2016a). Another notable feature is the occurrence of the 10 Å phase in a large pressure range of 9–22 GPa, corresponding to the stability field of the 3.65 Å phase (Fig. 1).

Discussion

The *in situ* experiments show the presence of chrysotile (and 'chrysotile-like' phases) in H_2O-saturated conditions up to about 500 °C at high pressure. Another new finding of the present study is the complex evolution of chrysotile with the formation of two intermediate 'chrysotile-like' phases II and III. 'Chrysotile-like' phase II appeared between 3.7 GPa / 260 °C and 5 GPa / 365 °C likely has a densified structure, as indicated by appreciable shifts of the diffraction peaks to higher diffraction angles 2θ (Figs. 3, 4, 5) and the decreased unit-cell volume (Fig. 8). The polymorphic character of the phase transition I–II observed in this study is consistent with the data of Hilairet et al. (2006), who reported a compression anomaly for chrysotile at 4.5–5 GPa (23 °C).

We also noted a broad low-angle reflection at $2\theta < 2°$, which appears in the chrysotile XRD pattern starting from 3.8 GPa / 215 °C (Fig. 4) and becomes more pronounced in phases II and III. This feature indicates the presence of a super-structure and disordering. This observation is similar to that observed in antigorite at about 300 °C (Perrillat et al. 2005). In particular, *in situ* H*P*–H*T* XRD patterns of antigorite contain a new peak at $d = 12.2$ Å ($2\theta = 2.8°$) and the diminished basal peak (001). The chrysotile peak (002) degradation is evident in the phase III XRD pattern (Figs. 3 and 4). Perrillat et al. (2005) suggested this low-angle reflection and other changes in the XRD patterns due to the structural modulation in antigorite described by a large supercell (Uehara and Kamata 1994; Groberty 2003). Interestingly, both chrysotile and antigorite exhibit apparently similar structural variations at moderate temperatures before decomposition. Comparing with chrysotile, antigorite are more stable and dehydrated at

mantle conditions (Bromiley and Pawley 2003; Proctor and Hirth 2016). Subduction seismic activity is often associated with serpentine dehydration (Hacker et al. 2003a, 2003b; Hilairet et al. 2007; Gasc et al. 2011, 2017).

Another new feature of the 'chrysotile-like' phase III is a pronounced increase of the interatomic / interlayer distances, compared to phase II, as characterized by a drastic shift of the diffraction peaks to lower angles (Figs. 3 and 5). Such increase in interlayer distances can be explained by over-hydration, analogous to that proceeding during the formation of the H*P* modification of talc, the 10 Å phase (Yamamoto and Akimoto 1977; Bauer and Sclar 1981; Wunder and Schreyer 1992), through the intercalation of H_2O molecules into the interlayer space (Chinnery et al. 1999; Fumagalli et al. 2001; Rashchenko et al. 2016b). In this context, it is interesting to mention the crystallization of the small amount of coesite along with the appearance of phase III at 405 °C / 5.25 GPa (Fig. 3). As we noted above, this is unlikely an effect of SiO_2 solubility change. Therefore, it is reasonable to relate the formation of excess silica and phase III. Previous spectroscopic studies have shown that H_2O intercalation into phyllosilicate structures, such as the 10 Å phase, is commonly accompanied by the creation of Si vacancies in the tetrahedral layer (Welch et al. 2006; Rashchenko et al. 2016a). Silanol groups associated with these vacancies are regarded as promoters of bonding interlayer water to the tetrahedral sheet, which is initially hydrophobic (Yang et al. 2005). The crystallization of both coesite and the phase III (Fig. 3) is consistent with the partial removal of Si from the chrysotile layer for H_2O incorporation into the latter.

The next step in the evolution of the 'chrysotile + water' system is the decomposition of the 'chrysotile-like' phase III to the 10 Å phase and forsterite starting at 500 °C / 5.8 GPa, in agreement with the data of long-term quench experiments (summarized in the review of Ulmer and Trommsdorff (1999) and presented in Fig. 1). In the presence of excess SiO_2 the formation of forsterite is immediately followed by its consumption to form enstatite. Remarkably, we found that the 10 Å phase and enstatite are competing product phases, and the amount of SiO_2 is sufficient to produce the 10 Å phase via reaction with forsterite. We suggest that the formation of enstatite is related to the lack of excess H_2O needed to form the 10 Å phase. This H_2O deficiency is confirmed by the absence of any ice in the XRD patterns collected on the *T* released after the completion of the experiments (Fig. 3, Table 1). This observation is also consistent with the evolution of the main XRD peak of coesite / stishovite at 2θ ~ 8° (Fig. 3): its intensity does not change upon temperature released down to 22 GPa / 125 °C. This result implies the deficiency or a complete absence of a liquid medium that could influence dissolution–precipitation of the SiO_2 phases.

Thus, there are several lines of evidence for the consumption of a significant part of excess H_2O in the course of the formation of the 10 Å phase, or probably even earlier during the formation of the 'chrysotile-like' phase III with extra H_2O in interlayers. Therefore, it is no surprise that when the *P*–*T* conditions become favourable for the '10 Å phase → 3.65 Å phase' transformation at 8.8 GPa / 500 °C (Pawley et al. 2011; Rashchenko et al. 2016a). This reaction remains incomplete due to the deficiency of water needed for the highly hydrous 3.65 Å phase. Consequently, the 10 Å and 3.65 Å phases coexist in a wide pressure range of 8–15 GPa, within the stability field of the 3.65 Å phase. This observation apparently confirms or even extends the H*P* stability range of the 3.65 Å and 10 Å phases. One plausible explanation for the expanded stability of the 3.65 Å and 10 Å phases is the incorporation of Al (and Fe) in our experiments. In addition, the presence of enstatite in association with these hydrous phases in our experiments (Fig. 3, Table 1) is interesting. Namely, it emphasizes a crucial role of the excess water on the stability of hydrous phases, especially the 3.65 Å phase with the largest water content (35 wt.%, Wunder et al. 2012).

Implications

The present study shows that chrysotile in water-saturated conditions exhibits higher thermal stability and undergoes more complicated phase transitions and dehydration processes than those suggested by previous studies. This has important implications for better understanding serpentine behavior in subduction zones and its roles in the transport of water into Earth's mantle. In particular, our experiments were mostly conducted under conditions corresponding to those of "cold" or "ultracold" subductions (Fig. 1; Peacock and Wang 1999; Syracuse et al. 2010).

The present study of the "chrysotile + water" system shows the formation of the 'chrysotile-like' phase III, representing a new example of H_2O intercalation into magnesium phyllosilicates under upper-mantle conditions. In addition, the present experiments are the first to demonstrate the *in situ* succession of the hydrous phases: *serpentine → 10 Å phase → 3.65*A *phase*. The 3.65 Å phase having the highest quantity of water among DHMS is particularly important for water transport to the deep mantle. The 3.65 Å phase was never synthesized from serpentines before the present study. Another interesting finding is the stabilization of the 10 Å phase against the 3.65 Å phase in the H_2O-deficient environment, thereby making the 10 Å phase even more favourable as the water carrier in the deep-Earth conditions, encompassing a broader pressure range than it was previously thought.

Dehydration of serpentines has been suggested to have significant importance into seismic processes in subduction zones (Dobson et al. 2002). The present study demonstrates that the presence and participation of excess water significantly complicate the serpentine dehydration process than suggested from previous studies, leading to an appearance

of known DHMS phases and possible other hydrous metastable phases, discussed here and in the literature, for instance, Mg-sursassite in peridotite (Bromiley and Pawley 2002). The bulk H_2O contents in the SiO_2–MgO–H_2O and SiO_2–Al_2O_3–MgO–H_2O systems have marked controls on the HP–HT conditions for the formation of specific hydrous phases. For example, several weight percents of H_2O are sufficient to form the 10 Å phase and phase A, but not the 3.65 Å phase (Ulmer and Trommsdorff 1995). According to Wunder (1998), the synthesis of magnesium silicates from gels at high *P*–*T* conditions leads to a large variety of DHMS phases, including the dominant phases of the humite group and phase A, whereas the 10 Å and 3.65 Å phases were not detected below 10.5 GPa at 500–1100 °C. However, the very large H_2O contents that are needed for the formation of the 3.65 Å phase (above ~ 15 wt.% in our experiment) are possible in shallow subduction zones but are rare in deep counterparts.

Acknowledgements This work was performed under the auspicious of the state assignment of IGM SB RAS supported by Ministry of Science and Higher Education of the Russian Federation. The Russian Foundation for Basic Research (project no.21-55-14001) is gratefully acknowledged. Authors thank S.V. Rashchenko for fruitful discussion on XRD diffraction patterns of the talc-water system. We thank SPring-8 Synchrotron Radiation Facilities and BLXU-10 beamline for providing the synchrotron beam-time. JST, SD and YP would like to thank Natural Science and Engineering Council Canada for the award of individual Discovery Grants.

References

Bassett WA, Shen AH, Bucknum M, Chou I-M (1993) A new diamond anvil cell for hydrothermal studies to 2.5 GPa and from –190 to 1200 °C. Rev Sci Instrum 64:2340–2345

Bauer JF, Sclar CB (1981) The 10 Å-phase in the system MgO-SiO_2-H_2O. Am Mineral 66:576–585

Borodina U, Goryainov S, Oreshonkov A, Shatskiy A, Rashchenko S (2020) Raman study of 3.65 Å phase MgSi(OH)6 under high pressure and the bands assignment. High Press Res 40:495–510

Bromiley GD, Pawley AR (2002) The high-pressure stability of Mg-sursassite in a model hydrous peridotite: a possible mechanism for the deep subduction of significant volumes of H_2O. Contrib Miner Petrol 142:714–723

Bromiley GD, Pawley AR (2003) The stability of antigorite in the systems MgO-SiO_2-H_2O (MSH) and MgO-Al_2O_3-SiO_2-H_2O (MASH): The effects of Al^{3+} substitution on high-pressure stability. Am Miner 88:99–108

Bruker AXS TOPAS V4: General profile and structure analysis software for powder diffraction data. User's Manual. Bruker AXS, Karlsruhe, Germany (2008)

Chernosky JV Jr, Berman RG, Bryndzia LT (1988) Stability, phase relations, and thermodynamic properties of chlorite and serpentine group minerals. Rev Mineral Geochem 19(1):295–346

Chinnery NJ, Pawley AR, Clark SM (1999) *In situ* observation of the formation of 10 Å phase from talc + H_2O at mantle pressures and temperatures. Science 286:940–942

Chollet M, Daniel I, Koga KT, Morard G, van de Moortele B (2011) Kinetics and mechanism of antigorite dehydration: implications for subduction zone seismicity. J Geophys Res Solid Earth 116:1–9

Cogulu E, Laurent R (1984) Mineralogical and chemical variations in chrysotile veins and peridotite host-rocks from the asbestos belt of southern Quebec. Canad Miner 22:173–183

Crichton WA, Ross NL (2000) Equation of state of phase E. Miner Mag 64:561–567

Dobson DP, Meredith PG, Boon SA (2002) Simulation of subduction zone seismicity by dehydration of serpentine. Science 298:1407–1410

Evans BW (2004) The serpentine multisystem revisited: Chrysotile is metastable. Intern Geol Rev 46:479–506

Fletcher NH (1970) The Chemical Physics of Ice. Cambridge University Press, London

Frost DJ, Fei Y (1998) Stability of Phase D at high pressure and high temperature. J Geophys Res 103:7463–7474

Fumagalli P, Poli S (2005) Experimentally determined phase relations in hydrous peridotites to 6.5 GPa and their consequences on the dynamics of subduction zones. J Petrol 46:555–578

Fumagalli P, Stixrude L, Poli S, Snyder D (2001) The 10 Å phase: A high-pressure expandable sheet silicate stable during subduction of hydrated lithosphere. Earth Planet Sci Lett 186:125–141

Gasc J, Schubnel A, Brunet F, Guillon S, Mueller H-J, Lathe C (2011) Simultaneous acoustic emissions monitoring and synchrotron X-ray diffraction at high pressure and temperature: calibration and application to serpentinite dehydration. Phys Earth Planet Inter 189:121–133

Gasc J, Hilairet N, Tony Y, Ferrand T, Schubnel A, Wang Y (2017) Faulting of natural serpentinite: Implications for intermediate-depth seismicity. Earth Planet Sci Lett 474:138–147

Ghosh S, Schmidt MW (2014) Melting of phase D in the lower mantle and implications for recycling and storage of H_2O in the deep mantle. Geochim Cosmochim Acta 145:72–88

Groberty B (2003) Polytypes and higher-order structures of antigorite: A TEM study. Am Miner 88:27–36

Hacker BR, Abers GA, Peacock SM (2003a) Subduction factory 1. Theoretical mineralogy, densities, seismic wave speeds, and H_2O contents. J Geophys Res Solid Earth 108(B1):2029

Hacker BR, Peacock SM, Abers GA, Holloway SD (2003b) Subduction factory 2. Are intermediate depth earthquakes in subducting slabs linked to metamorphic dehydration reactions? J Geophys Res Solid Earth 108(B1):2030

Hammersley AP, Svensson SO, Hanfland M, Fitch AN, Häusermann D (1996) Two dimensional\detector software: From real detector to idealised image or two-theta scan. High Press Res 14:235–248

Hernandez J-A, Caracas R (2018) Proton dynamics and the phase diagram of dense water ice. J Chem Phys 148:214501

Hilairet N, Daniel I, Reynard B (2006) P-V equations of state and the relative stabilities of serpentine varieties. Phys Chem Miner 33:629–637

Hilairet N, Reynard B, Wang YB, Daniel I, Merkel S, Nishiyama N, Petitgirard S (2007) High pressure creep of serpentine, interseismic deformation, and initiation of subduction. Science 318:1910–1913

Hirao N, Kawaguchi SI, Hirose K, Shimizu K, Ohtani E, Ohishi Y (2020) New developments in high-pressure X-ray diffraction beamline for diamond anvil cell at SPring-8. Matter Radiat. Extremes 5. Art 018403:1–10

Holl CM, Smyth JR, Manghnani MH, Amulele GM, Sekar M, Frost DJ, Prakapenka VB, Shen G (2006) Crystal structure and compression of an iron-bearing Phase A to 33 GPa. Phys Chem Miner 33:192–199

Inoue T, Yoshimi I, Yamada A, Kikegawa T (2009) Time-resolved X-ray diffraction analysis of the experimental dehydration of serpentine at high pressure. J Miner Petrol Sci 104:105–109

Kanzaki M (1991) Stability of hydrous magnesium silicates in the mantletransition zone. Phys Earth Planet Inter 66:307–312

Komabayashi T, Omori S (2006) Internally consistent thermodynamic data set for dense hydrous magnesium silicates up to 35 GPa, 1600 ℃: Implications for water circulation in the Earth's deep mantle. Phys Earth Planet Inter 156:89–107

Kudoh Y, Inoue T (1999) Mg-vacant structural modules and dilution of the symmetry of hydrous wadsleyite, β-$Mg_{2-x}SiH_{2x}O_4$ with 0.00 ≤ x ≤ 0.25. Phys Chem Miner 26:382–388

Liu X, Matsukage KN, Nishihara Y, Suzuki T, Takahashi E (2019) Stability of the hydrous phases of Al-rich phase D and Al-rich phase H in deep subducted oceanic crust. Am Mineral 104:64–72

Mao HK, Xu J, Bell PM (1986) Calibration of the ruby pressure gauge to 800 kbar under quasihydrostatic conditions. J Geophys Res Solid Earth 91:4673–4676

Mellini M, Trommsdorff V, Compagnoni R (1987) Antigorite polysomatism: behaviour during progressive metamorphism. Contrib Miner Petrol 97:147–155

Mookherjee M, Speziale S, Marquardt H, Jahn S, Wunder B, Koch-Muller M, Liermann HP (2015) Equation of state and elasticity of the 3.65 Å phase: Implications for the X-discontinuity. Am Miner 100:2199–2208

Nestola F, Angel RJ, Zhao J, Garrido CJ, Sanchez-Vizcaino VL, Capitani G, Mellini M (2010) Antigorite equation of state and anomalous softening at 6 GPa: An *in situ* single-crystal X-ray diffraction study. Contrib Miner Petrol 160:33–43

Ohira I, Ohtani E, Sakai T, Miyahara M, Hirao N, Ohishi Y, Nishijima M (2014) Stability of a hydrous δ-phase, AlOOH-$MgSiO_2(OH)_2$, and a mechanism for water transport into the base of lower mantle. Earth Planet Sci Lett 401:12–17

Ohtani E (2015) Hydrous minerals and the storage of water in the deep mantle. Chem Geol 418:6–15

Ohtani E, Litasov K, Hosoya T, Kubo T, Kondo T (2004) Water transport into the deep mantle and formation of a hydrous transition zone. Phys Earth Planet Inter 143:255–269

Ohtani E, Yuan L, Ohira I, Shatskiy A, Litasov K (2018) Fate of water transported into the deep mantle by slab subduction. J Asian Earth Sci 167:2–10

Pamato MG, Myhill R, BoffaBallaran T, Frost DJ, Heidelbach F, Miyajima N (2015) Lower-mantle water reservoir implied by the extreme stability of a hydrous aluminosilicate. Nat Geosci 8:75–79

Pawley AR, Wood BJ (1995) The high-pressure stability of talc and 10 Å phase: Potential storage sites for H_2O in subduction zones. Am Mineral 80:998–1003

Pawley AR, Chinnery NJ, Clark SM, Walter MJ (2011) Experimental study of the dehydration of 10 Å phase, with implications for its H_2O content and stability in subducted lithosphere. Contrib Miner Petrol 162:1279–1289

Peacock SM, Wang K (1999) Seismic consequences of warm versus cool subduction metamorphism: Examples from Southwest and Northeast Japan. Science 286:937–939

Perrillat J-P, Daniel I, Koga KT, Reynard B, Cardon H, Crichton WA (2005) Kinetics of antigorite dehydration: A real-time X-ray diffraction study. Earth Planet Sci Lett 236:899–913

Proctor B, Hirth G (2016) "Ductile to brittle" transition in thermally stable antigorite gouge at mantle pressures. J Geophys Res Solid Earth 121:1652–1663

Rashchenko SV, Kamada S, Hirao N, Litasov KD, Ohtani E (2016a) *In situ* X-ray observation of 10 Å phase stability at high pressure. Am Mineral 101:2564–2569

Rashchenko SV, Likhacheva AY, Goryainov SV, Krylov AS, Litasov KD (2016b) *In situ* spectroscopic study of water intercalation into talc: New features of 10 Å phase formation. Am Mineral 101:431–436

Schmidt MW, Poli S (1998) Experimentally based water budgets for dehydrating slabs and consequences for arc magma generation. Earth Planet Sci Lett 163:361–379

Sclar CB, Morzenti SP (1971) High pressure synthesis and geophysical significance of a new hydrous phase in the system MgO-SiO_2-H_2O. Geol Soc Am Abstract Prog 3:698

Sclar CB, Carrison LC, Schwartz CM (1965) Phase equilibria in the system MgO-SiO_2-H_2O, 20–130 kbar, 350–1300 °C. Am Ceram Soc Bull 44(8):634

Sokolova TS, Dorogokupets PI, Litasov KD (2013) Self-consistent pressure scales based on the equations of state for ruby, diamond, MgO, B2–NaCl, as well as Au, Pt, and other metals to 4 Mbar and 3000 K. Russ Geol Geophys 54:181–199

Syracuse EM, van Keken PE, Abers GA (2010) The global range of subduction zone thermal models. Phys Earth Planet Inter 183:73–90

Uehara S, Kamata K (1994) Antigorite with a large supercell from Saganoseki, Oita Prefecture, Japan. Can Miner 32(1):93–103

Ulmer P, Trommsdorff V (1999) Phase relations of hydrous mantle subducting to 300 km. In: Fei Y, Bertka CM, Mysen BO (eds), Mantle Petrology: Field Observations and High Pressure Experimentation: a Tribute to Francis R(Joe) Boyd. Geochem Soc Spec Public 6:259–281

Ulmer P, Trommsdorff V (1995) Serpentine stability to mantle depths and subduction-related magmatism. Science 268:858–861

Welch MD, Wunder B (2012) A single-crystal X-ray diffraction study of the 3.65 Å phase $MgSi(OH)_6$, a high-pressure hydroxide-perovskite. Phys Chem Miner 39:693–697

Welch MD, Pawley AR, Ashbrook SE, Mason HE, Phillips BL (2006) Si vacancies in the 10 Å phase. Am Miner 91:1707–1710

Wicks FJ, O'Hanley DS (1988) Serpentine minerals: structures and petrology. In: Bailey SW (ed) Hydrous Phyllosilicates: (exclusive of micas). Mineralogy Society of America, Washington DC, Vol 19, pp 91–188

Wunder B (1998) Equilibrium experiments in the system MgO–SiO_2–H_2O (MSH): stability fields of clinohumite-OH [$Mg_9Si_4O_{16}(OH)_2$], chondrodite-OH [$Mg_5Si_2O_8(OH)_2$] and phase A($Mg_7Si_2O_8(OH)_6$). Contrib Miner Petrol 132(2):111–120

Wunder B, Schreyer W (1992) Metastability of 10 Å-phase in the system MgO-SiO_2-H_2O (MSH). What about hydrous MSH phases in subduction zones? J Petrol 33(4):877–889

Wunder B, Schreyer W (1997) Antigorite: high pressure stability in the system MgO-SiO_2-H_2O (MSH). Lithos 41:213–227

Wunder B, Wirth R, Koch-Muller M (2011) The 3.65 Å phase in the system MgO-SiO_2-H_2O: Synthesis, composition, and structure. Am Miner 96:1207–1214

Wunder B, Jahn S, Koch-Muller M, Speziale S (2012) The 3.65 Å phase, $MgSi(OH)_6$: Structural insights from DFT-calculations and T-dependent IR spectroscopy. Am Mineral 97:1043–1048

Yamamoto K, Akimoto S (1977) The system MgO-SiO_2-H_2O at high pressures and temperatures – stability field for hydroxyl-chondrodite, hydroxyl-clinohumite and 10 Å phase. Am J Sci 277:288–312

Yang H, Prewitt CT, Frost DJ (1997) Crystal structure of the dense hydrous magnesium silicate, phase D. Am Miner 82:651–654

Yang J, Meng S, Xu L, Wang EG (2005) Water adsorption on hydroxylated silica surfaces studied using the density functional theory. Phys Rev B 71:035413